

Targeting One- and Two-Dimensional Ta–Te Structures via Nanotube Encapsulation

Scott Stonemeyer,[#] Mehmet Dogan,[#] Jeffrey D. Cain, Amin Azizi, Derek C. Popple, Austin Culp, Chengyu Song, Peter Ercius, Marvin L. Cohen, and Alex Zettl^{*}

Cite This: *Nano Lett.* 2022, 22, 2285–2292

Read Online

ACCESS |

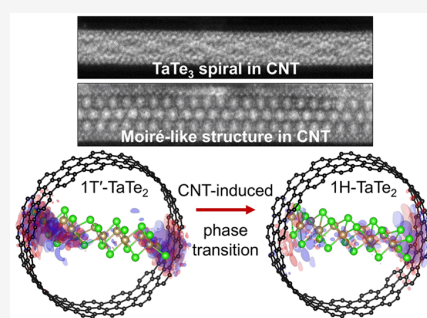
Metrics & More

Article Recommendations

Supporting Information

ABSTRACT: Fine control over material synthesis on the nanoscale can facilitate the stabilization of competing crystalline structures. Here, we demonstrate how carbon nanotube reaction vessels can be used to selectively create one-dimensional TaTe₃ chains or two-dimensional TaTe₂ nanoribbons with exquisite control of the chain number or nanoribbon thickness and width. Transmission electron microscopy and scanning transmission electron microscopy reveal the detailed atomic structure of the encapsulated materials. Complex superstructures such as multichain spiraling and apparent multilayer moirés are observed. The rare 2H phase of TaTe₂ (1H in monolayer) is found to be abundant as an encapsulated nanoribbon inside carbon nanotubes. The experimental results are complemented by density functional theory calculations for the atomic and electronic structure, which uncovers the prevalence of 2H-TaTe₂ due to nanotube-to-nanoribbon charge transfer and size confinement. Calculations also reveal new 1T' type charge density wave phases in TaTe₂ that could be observed in experimental studies.

KEYWORDS: One-dimensional materials, two-dimensional materials, nanoribbons, transition metal dichalcogenides, scanning transmission electron microscopy, nanotubes



1. INTRODUCTION

Isolating specific stoichiometries and structures of materials is a key goal of material property design and control. Transition metal chalcogenides of the form MX_n, with M a transition metal, X a chalcogen, and *n* typically an integer, are enjoying a resurgence in popularity for fundamental science study and applications including field-effect transistors, photodetectors, catalysts, and optoelectronics.^{1–7} The materials can assume an abundance of different stoichiometries and structures, but two of the more popular configurations are the transition metal dichalcogenides (TMDs) with *n* = 2 and the transition metal trichalcogenides (TMTs) with *n* = 3. TMTs are typically chainlike exhibiting quasi-one-dimensional physical and electronic structure, while TMDs are typically sheetlike with quasi-two-dimensional structure.

Many M–X combinations readily adopt independently the TMD and TMT stoichiometry, as exemplified by the well-known compounds TiS₂ and TiSe₃, NbSe₂ and NbSe₃, and HfTe₂ and HfTe₃. For these materials, obtaining a specific stoichiometry, that is, selecting either TMD or TMT, is easily achieved by adjusting the reaction temperature and stoichiometric loading of reagents.^{8–10} On the other hand, some M–X combinations are not so easily separated into TMD or TMT, as is the case for tantalum telluride (Ta–Te). Scant previous reports comment on the overall crystalline structure of TaTe_n compounds, alluding to the fact that they are low-dimensional

structures similar to other members of the TMD and TMT family, but difficulty in isolating specific phases from the Ta–Te system via temperature or precursor loading has prevented significant further study.^{9,11}

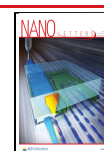
Recent developments in MX_n stabilization and isolation via nanotube encapsulation demonstrate that a physically confining carbon nanotube (CNT) or boron nitride nanotube (BNNT) “reaction vessel” affords an additional powerful synthesis control parameter for the selection of a specific stoichiometry.^{12,13} Indeed, the method has allowed for the stabilization of previously unknown MX_n stoichiometries and crystal structures,^{14–18} leading to novel electrical and optical properties.^{19,20}

Here, we report the successful targeted isolation of TaTe₃ and TaTe₂ via CNT encapsulation. The specific stoichiometry can be preferentially selected by choosing the proper nanotube inner diameter and overall reaction temperature of the synthesis. Encapsulation provides not only greater experimental control over the obtained structure, but once the materials

Received: November 30, 2021

Revised: March 4, 2022

Published: March 10, 2022



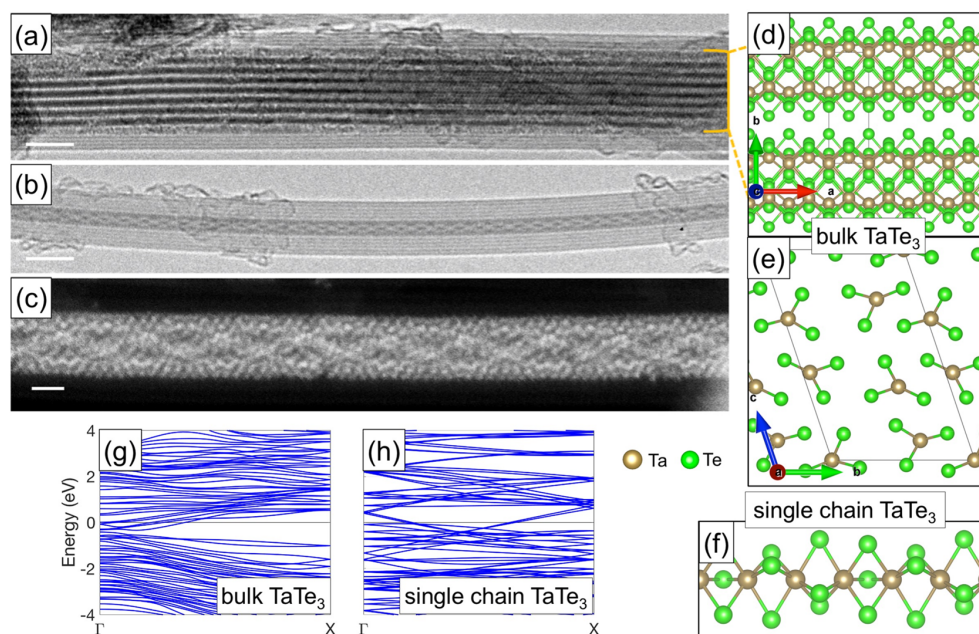


Figure 1. Electron microscopy images of encapsulated TaTe_3 chains. (a) TEM image of multichain TaTe_3 encapsulated in a 9.4 nm inner diameter CNT. The numerous parallel chains essentially constitute bulk TaTe_3 . (b,c) TEM and STEM images of spiraling few-chain TaTe_3 , encapsulated in 2.2 and 2.6 nm inner diameter CNT, respectively. Scale bars measure (a,b) 5 nm and (c) 1 nm. (d,e) Atomic model for bulk TaTe_3 , with a side view (d) and end view (e) of the trigonal prismatic chains. (f) Atomic model for single chain TaTe_3 . Ta and Te atoms are represented by gold and green spheres, respectively. (g,h) Electronic band structure of bulk (g) and single chain (h) TaTe_3 , computed with spin–orbit coupling. The zero of the energy is set to the Fermi level.

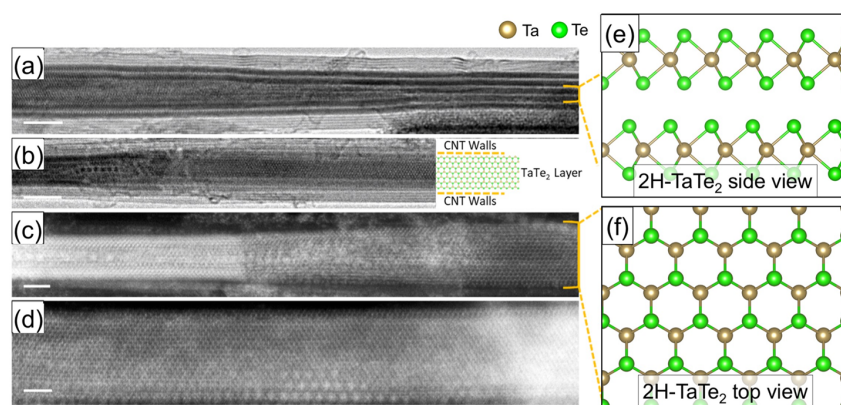


Figure 2. Electron microscopy images of encapsulated TaTe_2 nanoribbons. (a) TEM image of a curling, multilayer NR. Layer edges are clearly visible on the right-hand side of the image. (b) TEM image of a monolayer NR. (c) STEM image of a monolayer NR. (d) STEM image of the basal plane of a flat monolayer NR. Scale bars measure (a,b) 5 nm and (c,d) 2 nm. (e) Atomic model of the edge view of 2H- TaTe_2 , which should approximate the structure of the layer edges in (a). (f) Atomic model of the top view of 1H- TaTe_2 , which corresponds to the structure in (c). Ta and Te atoms are represented by gold and green spheres, respectively.

are formed it facilitates further characterization without the deleterious effects of rapid oxidation. We find not only excellent reproducibility for creating “expected” phases of TaTe_n (including TMT chain spiraling), but the method yields intriguing and completely new Ta–Te configurations, such as a moiré-interference-like structure whose detailed atomic configuration has yet to be determined. We complement our experimental studies with first-principles theoretical calculations to reveal the electronic structure of the newly isolated TaTe_3 and TaTe_2 phases and to gain further insight into

confinement size-effects on the electronic structure of TMD materials generally.

2. SYNTHESIS

Truncating 2D TMD materials at low layer number and 1D TMT materials to low chain number via nanotube encapsulation is facilitated by the inherent hierarchical crystal structure. Figures 1 and 2 present calculated atomic structures of the TaTe_3 and TaTe_2 species, respectively, highlighting the vdW nature of the crystalline materials. The weak vdW structure of the crystal allows for isolation within the CNT of

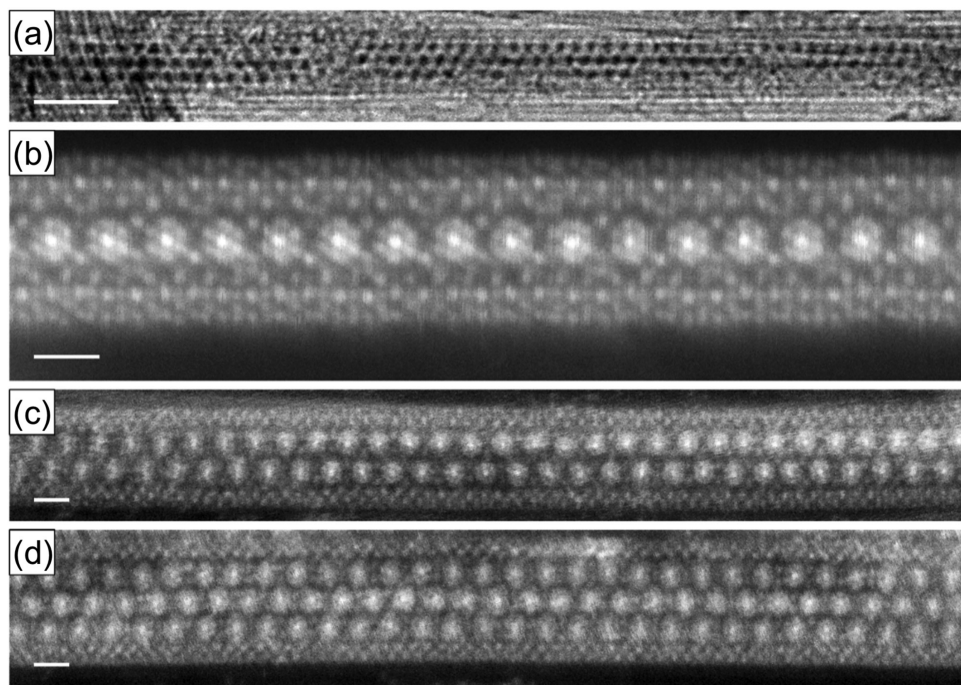


Figure 3. Electron microscopy images of the encapsulated moiré-like TaTe species. (a) TEM image of the moiré-like structure about three patterns wide. (b–d) STEM images of the moiré-like structure from increasing widths from a single pattern, double pattern, and triple pattern wide, respectively. Scale bars measure (a) 5 nm and (b–d) 1 nm.

the 2D sheets as few-layer or monolayer nanoribbons (NRs) and 1D chains down to few-chains or the single-chain limit. The encapsulation can also stabilize some crystal structures that are inherently unstable in bulk form (and have thus previously not been successfully synthesized).

Encapsulated TaTe₂ NRs, TaTe₃ chains, and TaTe_y moiré-like structures are synthesized within CNTs using a procedure similar to that used previously for the growth of confined TaS₂, NbSe₃, and HfTe₃.^{15,18,21} For TaTe₂ and TaTe₃, stoichiometric quantities of Ta powder and Te shot (~450 mg total), 1–2 mg of opened multiwalled CNTs with inner diameter ranging from 1.0 to 10.0 nm (CheapTubes, 90% SW-DW CNT), and ~5 mg/cm³ (ampule volume) of I₂ are sealed under vacuum (~10^{−6} Torr) in a quartz ampule. The TaTe_y moiré structures can be synthesized following the stoichiometry and loading of TaTe₂. The ampule is heated in a single-zone furnace at 600–900 °C for 3 days, then cooled to room temperature over 1–5 days.

Selectively synthesizing the TMT form of TaTe_n, that is, TaTe₃, is achieved by using an overall reaction temperature near 600 °C. Selecting the TMD form, that is, TaTe₂, is achieved through higher reaction temperatures, ranging from 800 to 900 °C, along with the moiré TaTe_y structure.

3. STRUCTURAL CHARACTERIZATION

Ta–Te filled CNTs are dispersed in isopropyl alcohol by bath sonication for 1 h and drop-cast onto lacey grids for transmission electron microscopy (TEM) and scanning transmission electron microscopy (STEM) imaging. TEM imaging is carried out on a JEOL 2010 microscope operated at 80 keV. STEM is carried out on the TEAM 0.5 microscope, a Titan 80–300 with an ultratwin pole piece gap, DCOR probe

aberration corrector, and is operated at 80 kV with semiconvergence angle of 30 mrad. STEM images are acquired using the ADF-STEM detector with an inner angle of 60 mrad and a beam current of approximately 70 pA.

TaTe₃ TMTs. Figure 1 presents selected TEM and STEM images for synthesized TMT TaTe₃. Figure 1a shows a multichain specimen encapsulated within a 9.4 nm inner diameter CNT. The lattice constants for bulk TaTe₃ have not been previously established to the best of our knowledge. In Figure 1d,e, we present computationally optimized structures for bulk TaTe₃ which has the Te atoms oriented in isosceles triangles perpendicular to the chain direction. The lattice constants along the *a*, *b*, and *c* directions are 3.72, 10.93, and 17.04 Å, respectively. Strong intrachain bonding is observed along the *a*-axis, while van der Waals gaps can be seen between the chains. These values are consistent with our experimental TEM and STEM observations. We have found this 24-atom phase by running a randomized search in unit cells with 4–48 atoms. In addition to being the configuration with the lowest energy, it is also dynamically stable, as presented in Figure S1a. We have computed this phonon spectrum using a 3 × 2 × 1 (144-atom) supercell via the frozen phonon method.

In other nanotube-encapsulated MX₃ systems, the trigonal prismatic chains often exhibit new structural configurations, such as on-chain torsional distortions or multichain spiraling.^{15,18} As shown in Figures 1b,c, we observe similar few-chain spiraling behavior for TaTe₃ encapsulated within a 2.2 and 2.6 nm inner diameter CNT, respectively. In Figure 1f, we present the theoretically relaxed atomic structure of single-chain TaTe₃, which adopts a geometry with equilateral triangles of Te atoms perpendicular to the chain direction with a periodicity of three TaTe₃ units and a lattice constant of 8.54 Å. The electronic band structures, including spin–orbit

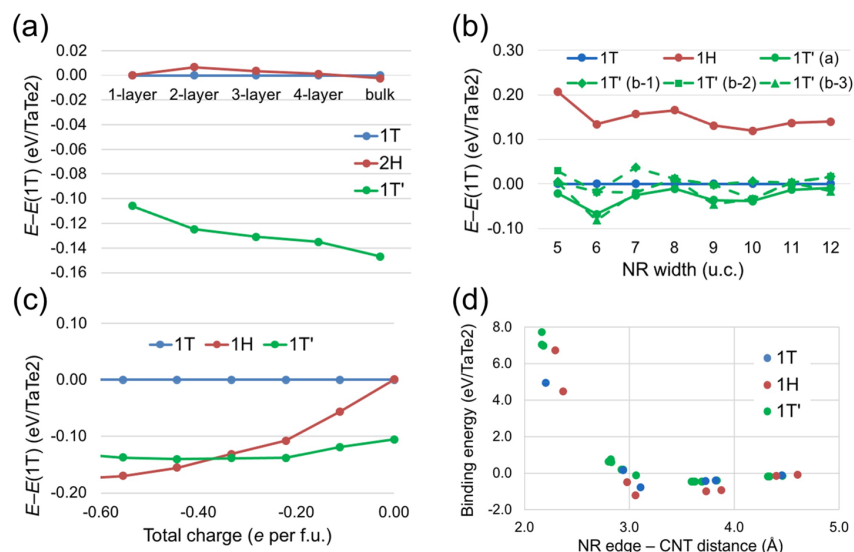


Figure 4. Energetic comparisons between the three main phases of TaTe₂. (a–c) Total energy with respect to 1T examined as a factor of (a) number of layers, (b) nanoribbon (NR) width, and (c) total charge. (d) For NRs encapsulated in carbon nanotubes (CNTs), the binding energy of each TaTe₂ configuration as a function of distance between the NR edge and the CNT inner walls.

coupling, for bulk and single chain TaTe₃, are presented in Figures 1g,h, and exhibit metallic behavior. The three-unit single chain structure is dynamically stable as shown in Figure S1b. To compare it with structures with different periodicities, we have run calculations with 1–6 TaTe₃ units in a cell, which all have higher energy than the three-unit structure (Figure S1c). The atomic and electronic structure of these configurations are presented in Figure S2.

TaTe₂ TMDs. Encapsulated TaTe₂ manifests itself as nanoribbons (NRs), where the width of the ribbon often just spans the inner diameter of the encapsulating CNT. The NRs can be composed of very few layers, most often as monolayers or bilayers. Similar behavior has been observed for other MX₂ encapsulated NRs.^{21,22} We note that at the elevated TMD reaction temperatures, no concomitant TMT specimens are observed, indicating that the encapsulation, coupled with higher temperatures, strongly favors the dichalcogenide phase of the TaTe system.

Figure 2 shows encapsulated TaTe₂ NRs in various projections. Figure 2a shows a 7.4 nm wide bilayer NR, which interestingly and somewhat unusually begins to fold in on itself (curl) at the edges due to the extreme confinement. Figure 2b–d shows examples of 5.0, 4.8, and 6.4 nm wide monolayer NR specimens, respectively. A closer look at these STEM images reveals that these NRs adopt the 2H phase in the monolayer, also called 1H (as highlighted in Figure 2c); for simplicity and clarity, the 2H phase is used as modeling in the side and plan view atomic models in Figure 2e,f. The curling observed in the multilayer specimen precludes the current study from assigning a polytype to the multilayer encapsulated NR. However, the energy differences between 1H-based polytypes (e.g., 2H vs 3R) is expected to be of the order of 0.01 eV,²³ much smaller than the energy difference between 2H and 1T' (>0.1 eV, as discussed below), so we continue the use of the 2H phase observed in the monolayer for atomic modeling of 1H-based multilayer TaTe₂.

Ta–Te Moiré-like Structures. In conjunction with TMD NRs observed at higher reaction temperatures, we find some

unexpected, yet fascinating structures stabilized within the CNT. The structure is not only stabilized in an encapsulated form but highly reproducible and transferrable to varying pattern widths. The patterns are moiré-like in appearance as observed in the projection plane. Figure 3 illustrates several examples of the moiré-like structure observed. Figure 3a shows a TEM image of a moiré-like structure roughly three patterns wide. Specimen ranging from a single pattern wide up to five patterns wide can be found in the sample with the moiré-type pattern retaining the same overall structure and spacing. Figure 3b–d shows the encapsulated moiré structure in increasing widths, that is, single, double, and triple pattern wide, respectively. The corresponding widths of these structures are 2.6, 3.1, and 3.6 nm, respectively, indicating that the moiré-like structure itself is roughly 0.5 nm in width and grows in a quantized fashion, requiring select CNTs of specific widths for each successive pattern added widthwise. Initial studies of these encapsulated patterned structures in previous work indicates these encapsulated structures are likely a core–shell entity.²⁴ This type of extended, coherent structure has not been observed in any highly confined material systems before. However, similar coherent structural patterns have been observed in layered TMD material systems, indicating these moiré-type structures could also arise from stacked layers of TaTe₂ inside of the CNT or a chiral TMD nanotube.²⁵ However, further investigation is required to elucidate the underlying atomic, and electronic structures of these moiré-like species.

4. DISCUSSION

The fact that the 2H (or 1H for monolayer) phase is experimentally observed for TaTe₂ NRs encapsulated in CNTs is unexpected, since TaTe₂ in bulk crystalline form is normally observed and reported in a distorted 1T phase (1T') that is obtained by a 3×1 reconstruction of the 1T phase.^{26–29} The only other experimental evidence of 2H-TaTe₂ that we are aware of is for a monolayer (1H) on bulk 1T'-TaTe₂.³⁰ The rarity of the 2H phase is consistent with the fact that it is 0.106

(0.147) eV/TaTe₂ higher in total energy than the 1T' in monolayer (bulk), as demonstrated in Figure 4a.

In order to investigate the potential mechanisms that lead to the stabilization of the 2H phase, we have conducted a series of DFT relaxations. To start with, the optimized configurations of the 1T, 1H and 1T' monolayers are obtained, which are presented in Figure S3a–c, respectively, along with their corresponding band structures that include the spin–orbit interaction. We find that the 1H monolayer is virtually degenerate with the 1T monolayer, whereas the 1T' monolayer is 106 meV/TaTe₂ unit lower in energy than the 1T phase, which is in agreement with previous calculations.³¹ The lattice parameter for the 1T and 1H phases are calculated as 3.69 and 3.67 Å, respectively, and for 1T' we find $a = 10.94$ Å, $b = 3.46$ Å, and $\gamma = 61.7^\circ$. The atomic and electronic structures of these phases are presented in Figure S3. In the bulk limit, we find the interlayer distance for the 1T, 2H, and 1T' phases to be 6.77, 6.88, and 6.64 Å, respectively.

The energetics of nanoribbons are expected to differ from the energetics of infinite layers. In order to explore these differences, we must first calculate the optimal configurations of TaTe₂ NRs in the three phases (1H, 1T, and 1T') from 5- to 12-unit cells (u.c.) wide. We have limited these calculations to zigzag NRs, as zigzag edges are experimentally observed in the STEM images in Figure 2. In constructing nanoribbons, considerations about the NR axis chosen and termination need to be made. In the lower symmetry 1T' phase, because the a and the b directions are inequivalent repeating along either direction yields different NR geometries (Figure S4 panel c vs panels d–f). Also, if the structure is repeated along the b direction then three NR geometries are possible for each width (Figure S4d–f). In addition to the NR axis chosen, various edge terminations are possible for each phase. For simplicity, we choose to keep the NRs stoichiometric, that is, the Te/Ta ratio remains 2:1. For stoichiometric NRs, in the case of the 1H phase the natural choice is to terminate one edge with Ta and the other edge with Te₂ (Figure S4b). In the 1T and 1T' cases, lowest energies are obtained when both edges are terminated with Te₂ (Figure S4a,c–f). We have compared this termination scheme to one where one edge is terminated with Ta and the other with Te₂ to find that it leads to energies that are a few tenths of an eV/TaTe₂ unit higher in energy for each NR. We present the relaxed, 6 u.c. wide NRs of all configurations of monolayer TaTe₂ in Figure S4.

We examine the energetics of these six different NR configurations in Figure 4b with the 1T NR energy set to zero. From Figures 4a and 3b, we find that when only taking geometry and size into consideration the NR favors the 1T phase in terms of its relative position in energy with respect to the other two phases. This is likely because the distortion of the atomic coordinates in 1T is smaller and more localized to the edges. In contrast, the 1H phase becomes disfavored as a NR, likely because of the more drastic distortions that occur especially at the Ta edge. We point out that in the limit of NR width going to infinity, the data points in Figure 4b should approach the leftmost data points in Figure 4a, and this trend does not visibly begin by the largest width we have considered. Thus, it is safe to say that the 1H phase will remain disfavored for the even wider NRs that are observed in the experiment. Therefore, NR edge effects and size alone cannot explain the favorability of the 1H phase experimentally observed in the carbon nanotubes, so we must examine other phenomena known to exist in encapsulated species, such as charge transfer.

When studying the energetics of charge transfer, it is important to notice the differences in the band structures of the 1H phase and the other two phases, as shown in Figure S3. As more electrons are added to the system, the tops of the valence bands that cross the Fermi energy in the 1H phase are filled. Such a large density of low energy states is not available for the 1T and 1T' phases. To check the effect of added charge on energetics, we have relaxed the three phases in 3×3 phases and added integer numbers of electrons. The resulting energy versus charge graph is presented in Figure 4c, which shows that the 1H phase is indeed favored in the electron rich environment and becomes the ground state when the system has an extra third of an electron per formula unit. Hence, if encapsulation by CNTs provides this electron rich environment, then the 1H phase NR is energetically preferred over the more commonly reported bulk 1T' phase.

In previous studies, encapsulated TMTs were found to gain electrons from the CNTs.^{18,32} To investigate the same possibility for TMD NRs, we have generated model TaTe₂–CNT systems where the armchair CNTs constrained the lattice constant of TaTe₂ NRs. We have taken 5, 6, and 7 u.c. wide nanoribbons and armchair CNTs with $m = n = 16, 17, 8$, and 19. Because the lattice constant of these CNTs, that is, 2.46 Å, is approximately two-thirds of the NR lattice constants, we have created simulation cells with 3 u.c. of CNT and 2 u.c. of TaTe₂ NRs. This has led to a total of 32 calculations with 222 to 270 atoms. To avoid even larger calculations, we have omitted 1T' (a) NRs and only included 1T' (b-1,2,3) NRs. To approximate the effect of compressive strain on CNTs, which is 0.9%, 0.5% and 6.3% for 1T, 1H, and 1T' NRs, respectively, we have increased their diameter proportionally, assuming a Poisson ratio of 0.2 based on the existing literature.^{33–38} To estimate the charge transfer between the CNTs and the NRs, we have simply calculated the electronic structure of these systems without attempting atomic relaxation. However, the results are instructive in terms of energetics as well. In Figure 4d, we plot the binding energy of each configuration as a function of the distance between the NR edge and the CNT. Here, the binding energy is defined as the total energy of the CNT+NR system minus the total energies of the CNT and NR systems separately and can be negative (attractive) or positive (repulsive). The NR–CNT distance is defined as half of the difference between the diameter of the CNT and the width of the NR. We find that the system is stable in this sense when the NR–CNT distance is 3 Å or larger. We also find that in the optimal 3 to 4 Å range, the 1H phase lies about 0.5 eV/f.u. lower in energy than the other phases. Thus, encapsulation alone favors the 1H phase NRs.

Finally, we have computed the charge transfer between the CNT and the NR in each case using the charge redistribution defined as $\Delta\rho(r, \phi, x) = \rho(\text{CNT} + \text{NR}) - \rho(\text{CNT}) - \rho(\text{NR})$, where the $\Delta\rho$ is expressed in terms of cylindrical coordinates with x being the coordinate along the periodic direction. Two examples of $\Delta\rho$ can be seen in Figure S5 which shows that the electron transfer occurs from the CNT to the NR, which is the case for all the calculations. To get the exact value of the electron transfer, Δq , we have plotted $\int_0^{2\pi} \int_0^a r \Delta\rho(r, \phi, x) dx d\phi$ as a function of r (where a is the lattice parameter) and integrated the result up to the value of r at which the integral changes sign. For the structures with a binding energy of 1 eV or less, we have found Δq to be in the range of 0.14 to 0.27 e per TaTe₂. This range of electron

transfer falls short of the $1/3 e$ per TaTe_2 calculated for the favorability of the 1H phase, however the $1/3 e$ per TaTe_2 is for an infinite layer. An electron transfer of $0.27 e$ per TaTe_2 falls roughly where the energetic favorability of the 1H and $1\text{T}'$ phase (in Figure 4c) are roughly equal. Therefore, the electron transfer combined with the favorability of the 1H phase NRs, given the preferred NR–CNT distance of 3–4 Å (Figure 4d), suffice to explain the abundance of 1H NRs observed in our experiments.

In our calculations on TaTe_2 monolayers, we have also discovered new $1\text{T}'$ -type charge density wave (CDW) phases, which are presented in Figure S6 along with the already known phases. We have found these phases by applying distortions similar to the one that produces the 3×1 $1\text{T}'$ phase from the 1T phase along both lattice directions. To confirm that these structures are dynamically stable, we have perturbed their atomic coordinates by random fractions of 0.2 Å in 6×6 unit cells and relaxed them (three times each). To the best of our knowledge, the configurations shown in Figure S6d–f have not been reported before (the 3×3 structure found in ref 31 has a different geometry). It is important to note that 3×3 CDW distortions have been observed in TaTe_2 experimentally, along with several other periodicities, so there is a need for computational work to pin down the exact atomic configurations of such phases.^{27–29} The electronic structures of these phases are presented in Figure S7, which demonstrate that the system reduces the density of states at the Fermi energy by allowing distortions in larger unit cells (or distortions with smaller q).

5. CONCLUSION

The TaTe system demonstrates significant material flexibility yet specificity in the encapsulation study presented above. Successful targeted synthesis of both TaTe_3 and TaTe_2 via encapsulation with CNT is discussed in detail with the specific stoichiometry of the TaTe system grown in the confined space within the CNT preferentially selected via the reaction temperature. Surprisingly, an unexpected 2H phase of the TaTe_2 NR is experimentally observed (1H in monolayer). DFT calculations uncover contributions of charge transfer and proximity of the encapsulated species to the CNT to alter the energetics of the TaTe_2 phases, accounting for the stability of the 2H phase as an encapsulated species. A new patterned structure exhibiting unique and fascinating moiré-like features is presented. Additional studies and examination of the unique patterned structure is required to elucidate the underlying atomic and electronic structure. However, the control shown in the encapsulated TaTe_x systems coupled with the unique structure and strong dependence of phase energetics as a function of size and energy transfer, further pushes the boundaries of material design and control at the nano- and atomic-scale.

■ ASSOCIATED CONTENT

SI Supporting Information

The Supporting Information is available free of charge at <https://pubs.acs.org/doi/10.1021/acs.nanolett.1c04615>.

Experimental details; computational details; phonon dispersions and energetics of TaTe_3 chains; atomic and electronic structures of the single chain TaTe_3 configurations with different periodicities; atomic and electronic structures of the three main phases of

monolayer TaTe_2 ; atomic structures of the studied TaTe_2 zigzag nanoribbons; spatial visualization of the electron transfer between the carbon nanotube and TaTe_2 nanoribbon; atomic structures of all distinct (meta)stable TaTe_2 monolayers found in this study; electronic band structure and densities of states (DOS) of all distinct (meta)stable TaTe_2 monolayers found in this study (PDF)

■ AUTHOR INFORMATION

Corresponding Author

Alex Zettl – Department of Physics, University of California at Berkeley, Berkeley, California 94720, United States; Materials Sciences Division, Lawrence Berkeley National Laboratory, Berkeley, California 94720, United States; Kavli Energy NanoSciences Institute at the University of California at Berkeley, Berkeley, California 94720, United States; Email: azettl@berkeley.edu

Authors

Scott Stonemeyer – Department of Physics, University of California at Berkeley, Berkeley, California 94720, United States; Department of Chemistry, University of California at Berkeley, Berkeley, California 94720, United States; Materials Sciences Division, Lawrence Berkeley National Laboratory, Berkeley, California 94720, United States; Kavli Energy NanoSciences Institute at the University of California at Berkeley, Berkeley, California 94720, United States; orcid.org/0000-0002-8135-5625

Mehmet Dogan – Department of Physics, University of California at Berkeley, Berkeley, California 94720, United States; Materials Sciences Division, Lawrence Berkeley National Laboratory, Berkeley, California 94720, United States; orcid.org/0000-0001-5414-362X

Jeffrey D. Cain – Department of Physics, University of California at Berkeley, Berkeley, California 94720, United States; Materials Sciences Division, Lawrence Berkeley National Laboratory, Berkeley, California 94720, United States; Kavli Energy NanoSciences Institute at the University of California at Berkeley, Berkeley, California 94720, United States; orcid.org/0000-0001-9244-4271

Amin Azizi – Department of Physics, University of California at Berkeley, Berkeley, California 94720, United States; Kavli Energy NanoSciences Institute at the University of California at Berkeley, Berkeley, California 94720, United States; orcid.org/0000-0001-9955-7228

Derek C. Popple – Department of Physics, University of California at Berkeley, Berkeley, California 94720, United States; Department of Chemistry, University of California at Berkeley, Berkeley, California 94720, United States; Materials Sciences Division, Lawrence Berkeley National Laboratory, Berkeley, California 94720, United States; Kavli Energy NanoSciences Institute at the University of California at Berkeley, Berkeley, California 94720, United States

Austin Culp – Department of Physics, University of California at Berkeley, Berkeley, California 94720, United States

Chengyu Song – National Center for Electron Microscopy, The Molecular Foundry, Lawrence Berkeley National Laboratory, Berkeley, California 94720, United States

Peter Ercius – National Center for Electron Microscopy, The Molecular Foundry, Lawrence Berkeley National Laboratory, Berkeley, California 94720, United States; orcid.org/0000-0002-6762-9976

Marvin L. Cohen — Department of Physics, University of California at Berkeley, Berkeley, California 94720, United States; Materials Sciences Division, Lawrence Berkeley National Laboratory, Berkeley, California 94720, United States

Complete contact information is available at:

<https://pubs.acs.org/10.1021/acs.nanolett.1c04615>

Author Contributions

*S.S. and M.D. contributed equally.

Author Contributions

S.S. and A.Z. conceived the idea; S.S. synthesized the materials; S.S., J.C., A.A., D.P., and A.C. performed electron microscopy data acquisition and analysis. M.D. and M.L.C. carried out density functional calculations. A.Z. and M.L.C. supervised the project; S.S., M.D., and A.Z. wrote the manuscript with input from all authors.

Notes

The authors declare no competing financial interest.

ACKNOWLEDGMENTS

This work was primarily funded by the U.S. Department of Energy, Office of Science, Office of Basic Energy Sciences, Materials Sciences and Engineering Division, under Contract No. DE-AC02-05-CH11231 within the sp²-Bonded Materials Program (KC2207) which provided for synthesis of the chains, structural characterization, and theoretical modeling of relaxed structure of the NRs. The elemental mapping work was funded by the U.S. Department of Energy, Office of Science, Office of Basic Energy Sciences, Materials Sciences and Engineering Division, under Contract No. DE-AC02-05-CH11231 within the van der Waals Heterostructures Program (KCWF16). Work at the Molecular Foundry (TEAM 0.5 characterization) was supported by the Office of Science, Office of Basic Energy Sciences, of the U.S. Department of Energy under Contract No. DE-AC02-05-CH11231. Support was also provided by the National Science Foundation under Grant DMR-1807233 which provided for preparation of opened nanotubes and Grant DMR 1926004 which provided for theoretical calculations of the electronic band structure of the materials. Computational resources were provided by the DOE at Lawrence Berkeley National Laboratory's NERSC facility and the NSF through XSEDE resources at NICS.

REFERENCES

- (1) Lopez-Sanchez, O.; Lembke, D.; Kayci, M.; Radenovic, A.; Kis, A. Ultrasensitive Photodetectors Based on Monolayer MoS₂. *Nat. Nanotechnol.* **2013**, *8*, 497.
- (2) Guo, J.; Li, F.; Sun, Y.; Zhang, X.; Tang, L. Oxygen-incorporated MoS₂ ultrathin nanosheets grown on graphene for efficient electrochemical hydrogen evolution. *J. Power Sources* **2015**, *291*, 195.
- (3) Island, J. O.; Molina-Mendoza, A. J.; Barawi, M.; Biele, R.; Flores, E.; Clamagirand, J. M.; Ares, J. R.; Sánchez, C.; Van Der Zant, H. S. J.; D'Agosta, R.; Ferrer, I. J.; Castellanos-Gomez, A. Electronics and Optoelectronics of Quasi-1D Layered Transition Metal Trichalcogenides. *2D Materials* **2017**, *4*, 022003.
- (4) Radisavljevic, B.; Radenovic, A.; Brivio, J.; Giacometti, V.; Kis, A. Single-Layer MoS₂ Transistors. *Nat. Nano* **2011**, *6*, 147.
- (5) Li, Y.; Li, Y.; Araujo, C. M.; Luo, W.; Ahuja, R. Single-Layer MoS₂ as Efficient Photocatalyst. *Catalysis Science and Technology* **2013**, *3*, 2214.
- (6) Wang, Q. H.; Kalantar-Zadeh, K.; Kis, A.; Coleman, J. N.; Strano, M. S. Electronics and Optoelectronics of Two-Dimensional Transition Metal Dichalcogenides. *Nat. Nanotechnol.* **2012**, *7*, 699.
- (7) Yang, T.; Lin, H.; Loh, K. P.; Jia, B. Fundamental Transport Mechanisms and Advancements of Graphene Oxide Membranes for Molecular Separation. *Chem. Mater.* **2019**, *31*, 1829.
- (8) Basuvalingam, S. B.; Zhang, Y.; Bloodgood, M. A.; Godiksen, R. H.; Curto, A. G.; Hofmann, J. P.; Verheijen, M. A.; Kessels, W. M. M.; Bol, A. A. Low-Temperature Phase-Controlled Synthesis of Titanium Di- And Tri-Sulfide by Atomic Layer Deposition. *Chem. Mater.* **2019**, *31*, 9354.
- (9) Revolinsky, E.; Brown, B.E.; Beerntsen, D.J.; Armitage, C.H. The Selenide and Telluride Systems of Niobium and Tantalum. *Journal of the Less Common Metals* **1965**, *8*, 63.
- (10) Brattas, L.; Kjekshus, A.; Rasmussen, S. E.; Svensson, S.; Koskikallio, J.; Kachi, S. The Non-Metal Rich Region of the Hf-Te System. *Acta Chem. Scand.* **1971**, *25*, 2783.
- (11) Brixner, L. H. Preparation and Properties of the Single Crystalline AB₂-Type Selenides and Tellurides of Niobium, Tantalum, Molybdenum and Tungsten. *Journal of Inorganic and Nuclear Chemistry* **1962**, *24*, 257.
- (12) Dai, J.; Li, M.; Zeng, X. C. Group IVB Transition Metal Trichalcogenides: A New Class of 2D Layered Materials beyond Graphene. *Wiley Interdisciplinary Reviews: Computational Molecular Science* **2016**, *6*, 211.
- (13) Manzeli, S.; Ovchinnikov, D.; Pasquier, D.; Zayzev, O. V.; Kis, A. 2D Transition Metal Dichalcogenides. *Nature Reviews Materials* **2017**, *2*, 17033.
- (14) Splendiani, A.; Sun, L.; Zhang, Y.; Li, T.; Kim, J.; Chim, C. Y.; Galli, G.; Wang, F. Emerging Photoluminescence in Monolayer MoS₂. *Nano Lett.* **2010**, *10*, 1271.
- (15) Meyer, S.; Pham, T.; Oh, S.; Ercius, P.; Kisielowski, C.; Cohen, M. L.; Zettl, A. Metal-Insulator Transition in Quasi-One-Dimensional HfTe₃ in the Few-Chain Limit. *Phys. Rev. B* **2019**, *100*, 041403.
- (16) Nagata, M.; Shukla, S.; Nakanishi, Y.; Liu, Z.; Lin, Y. C.; Shiga, T.; Nakamura, Y.; Koyama, T.; Kishida, H.; Inoue, T.; Kanda, N.; Ohno, S.; Sakagawa, Y.; Suenaga, K.; Shinohara, H. Isolation of Single-Wired Transition-Metal Monochalcogenides by Carbon Nanotubes. *Nano Lett.* **2019**, *19*, 4845.
- (17) Pham, T.; Oh, S.; Stonemeyer, S.; Shevitski, B.; Cain, J. D.; Song, C.; Ercius, P.; Cohen, M. L.; Zettl, A. Emergence of Topologically Nontrivial Spin-Polarized States in a Segmented Linear Chain. *Phys. Rev. Lett.* **2020**, *124*, 20.
- (18) Pham, T.; Oh, S.; Stetz, P.; Onishi, S.; Kisielowski, C.; Cohen, M. L.; Zettl, A. Torsional Instability in the Single-Chain Limit of a Transition Metal Trichalcogenide. *Science* **2018**, *361*, 263.
- (19) Zhang, J.-J.; Guan, J.; Dong, S.; Yakobson, B. I. Room-Temperature Ferroelectricity in Group-IV Metal Chalcogenide Nanowires. *J. Am. Chem. Soc.* **2019**, *141*, 15040.
- (20) Kashitban, R. J.; Burdanova, M. G.; Vasylenko, A.; Wynn, J.; Medeiros, P. V. C.; Ramasse, Q.; Morris, A. J.; Quigley, D.; Lloyd-Hughes, J.; Sloan, J. Linear and Helical Cesium Iodide Atomic Chains in Ultranarrow Single-Walled Carbon Nanotubes: Impact on Optical Properties. *ACS Nano* **2021**, *15*, 13389.
- (21) Cain, J. D.; Oh, S.; Azizi, A.; Stonemeyer, S.; Dogan, M.; Thiel, M.; Ercius, P.; Cohen, M. L.; Zettl, A. Ultranarrow TaS₂ Nanoribbons. *Nano Lett.* **2021**, *21*, 3211.
- (22) Wang, Z.; Li, H.; Liu, Z.; Shi, Z.; Lu, J.; Suenaga, K.; Joung, S. K.; Okazaki, T.; Gu, Z.; Zhou, J.; Gao, Z.; Li, G.; Sanvito, S.; Wang, E.; Iijima, S. Mixed Low-Dimensional Nanomaterial: 2D Ultranarrow MoS₂ Inorganic Nanoribbons Encapsulated in Quasi-1D Carbon Nanotubes. *J. Am. Chem. Soc.* **2010**, *132*, 13840.
- (23) Azizi, A.; Dogan, M.; Cain, J. D.; Lee, K.; Yu, X.; Shi, W.; Glazer, E. C.; Cohen, M. L.; Zettl, A. Experimental and Theoretical Study of Possible Collective Electronic States in Exfoliable Re-Doped NbS₂. *ACS Nano* **2021**, *15*, 18297.
- (24) Pelz, P. M.; Brown, H. G.; Stonemeyer, S.; Findlay, S. D.; Zettl, A.; Ercius, P.; Zhang, Y.; Ciston, J.; Scott, M. C.; Ophus, C. Phase-Contrast Imaging of Multiply-Scattering Extended Objects at Atomic Resolution by Reconstruction of the Scattering Matrix. *Physical Review Research* **2021**, *3*, 1.

- (25) Zhao, X.; Qiao, J.; Chan, S. M.; Li, J.; Dan, J.; Ning, S.; Zhou, W.; Quek, S. Y.; Pennycook, S. J.; Loh, K. P. Unveiling Atomic-Scale Moiré Features and Atomic Reconstructions in High-Angle Commensurately Twisted Transition Metal Dichalcogenide Homobilayers. *Nano Lett.* **2021**, *21*, 3262.
- (26) Brown, B. E. The Crystal Structures of NbTe₂ and TaTe₂. *Acta Crystallogr.* **1966**, *20*, 264.
- (27) Feng, J.; Tan, A.; Wagner, S.; Liu, J.; Mao, Z.; Ke, X.; Zhang, P. Charge Modulation and Structural Transformation in TaTe₂ Studied by Scanning Tunneling Microscopy/Spectroscopy. *Appl. Phys. Lett.* **2016**, *109*, 021901.
- (28) Liu, Y.; Shao, D. F.; Li, L. J.; Lu, W. J.; Zhu, X. D.; Tong, P.; Xiao, R. C.; Ling, L. S.; Xi, C. Y.; Pi, L.; Tian, H. F.; Yang, H. X.; Li, J. Q.; Song, W. H.; Zhu, X. B.; Sun, Y. P. Nature of Charge Density Waves and Superconductivity in 1T-TaSe₂-XTex. *Phys. Rev. B* **2016**, *94*, 045131.
- (29) Wei, L. L.; Sun, S. S.; Sun, K.; Liu, Y.; Shao, D. F.; Lu, W. J.; Sun, Y. P.; Tian, H. F.; Yang, H. X. Charge Density Wave States and Structural Transition in Layered Chalcogenide TaSe_{2-x}Tex. *Chin. Phys. Lett.* **2017**, *34*, 086101.
- (30) Kar, I.; Dolui, K.; Harnagea, L.; Kushnirenko, Y.; Shipunov, G.; Plumb, N. C.; Shi, M.; Büchner, B.; Thirupathiah, S. Experimental Evidence of a Stable 2 H Phase on the Surface of Layered 1 T'-TaTe₂. *J. Phys. Chem. C* **2021**, *125*, 1150.
- (31) Miller, D. C.; Mahanti, S. D.; Duxbury, P. M. Charge Density Wave States in Tantalum Dichalcogenides. *Phys. Rev. B* **2018**, *97*, 045133.
- (32) Stonemeyer, S.; Cain, J. D.; Oh, S.; Azizi, A.; Elasha, M.; Thiel, M.; Song, C.; Ercius, P.; Cohen, M. L.; Zettl, A. Stabilization of NbTe₃, VTe₃, and TiTe₃ via Nanotube Encapsulation. *J. Am. Chem. Soc.* **2021**, *143*, 4563.
- (33) Yakobson, B. I.; Brabec, C. J.; Bernholc, J. Nanomechanics of Carbon Tubes: Instabilities beyond Linear Response. *Phys. Rev. Lett.* **1996**, *76*, 2511.
- (34) Lu, J. P. Elastic Properties of Carbon Nanotubes and Nanoropes. *Phys. Rev. Lett.* **1997**, *79*, 1297.
- (35) Hernández, E.; Goze, C.; Bernier, P.; Rubio, A. Elastic Properties of C and BxCyNy Composite Nanotubes. *Phys. Rev. Lett.* **1998**, *80*, 4502.
- (36) Popov, V.; Van Doren, V.; Balkanski, M. Elastic Properties of Single-Walled Carbon Nanotubes. *Physical Review B - Condensed Matter and Materials Physics* **2000**, *61*, 3078.
- (37) Kudin, K. N.; Scuseria, G. E.; Yakobson, B. I. $\{C\}_2\{F\}$, BN, and C Nanoshell Elasticity from Ab Initio Computations. *Phys. Rev. B* **2001**, *64*, 235406.
- (38) Gupta, S.; Dharamvir, K.; Jindal, V. K. Elastic Moduli of Single-Walled Carbon Nanotubes and Their Ropes. *Physical Review B - Condensed Matter and Materials Physics* **2005**, *72*, 165428.

Recommended by ACS

Hexagonal Boron Nitride Crystal Growth from Iron, a Single Component Flux

Jiahua Li, James H. Edgar, *et al.*

APRIL 05, 2021
ACS NANO

READ 

Charge-Density-Wave Thin-Film Devices Printed with Chemically Exfoliated 1T-TaS₂ Ink

Saba Baraghani, Alexander A. Balandin, *et al.*

MARCH 24, 2022
ACS NANO

READ 

Liquid-Phase Exfoliation of Magnetically and Optoelectronically Active Ruthenium Trichloride Nanosheets

David Lam, Mark C. Hersam, *et al.*

JUNE 17, 2022
ACS NANO

READ 

"Missing" One-Dimensional Red-Phosphorus Chains Encapsulated within Single-Walled Carbon Nanotubes

D. V. Rybkovskiy, C. P. Ewels, *et al.*

APRIL 04, 2022
ACS NANO

READ 

Get More Suggestions >